Controlling the optical pathlength in continuous-wave reflectance spectroscopy using polarization

Callum M Macdonald, Susmita Sridhar, Hung T X Do, Javier Luna-Labrador, Mouloud Adel, Anabela da Silva

Research Article | Vol. 12, No. 7 / 1 July 2021 / Biomedical Optics Express 4401
Biomedical Optics EXPRESS

Controlling the optical pathlength in continuous-wave reflectance spectroscopy using polarization

CALLUM M. MACDONALD,[1,2,*] SUSMITA SRIDHAR,[1] HUNG T. X. DO,[1] JAVIER LUNA-LABRADOR,[1] MOULOUD ADEL,[1] AND ANABELA DA SILVA[1]

[1]Aix Marseille Univ, CNRS, Centrale Marseille, Institut Fresnel, Marseille, France
[2]Department of Medical Physics and Biomedical Engineering, University College London, Gower Street, London WC1E 6BT, UK
[*]callum.macdonald@ucl.ac.uk

Abstract: We investigate potential improvements of continuous-wave diffuse reflectance spectroscopy within highly scattering media by employing polarization gating. Simulations are used to show the extent at which the effective optical pathlength varies in a typical scattering medium as a function of the optical wavelength, the total level of absorption, and the selected polarization channels, including elliptical and circular polarization channels. Experiments then demonstrate that a wavelength dependent polarization gating scheme may reduce the prior knowledge required to solve the problem of chromophore quantification. This is achieved by finding combinations of polarization channels which have similar effective optical pathlengths through the medium at each wavelength.

1. Introduction

Polarization sensitive image analysis offers unique capabilities for biomedical applications, such as the ability to isolate or remove surface layer reflections to improve visibility [1], or as a means of tissue characterization for diagnostic or monitoring purposes [2,3]. In order to fully exploit polarization effects, they must first be well understood. A particularly relevant detail is that of the depolarization rate (as a function of propagation distance within a medium), and its relationship to the effective probing volume when imaging with specific polarization filtering or "gating" channels. Early investigations into this topic demonstrated surprising differences between depolarization rates for circular and linear polarization channels in certain types of scattering media [4,5]. Subsequent investigations have revealed a complicated dependence on factors which include the shape, size distribution, and refractive index of scattering particles within a medium [6–9]. This extends to observations in various biological tissues, which can exhibit significantly different polarization responses when compared to common tissue phantom materials, even those with similar bulk optical properties [10–12].

One important application for polarization sensitive imaging is in the spectroscopic examination of biological tissues. Spectroscopy involves the quantitative analysis of chromophores by measuring the wavelength dependent attenuation of light which has propagated through a sample. In a biomedical context, this can provide information such as blood oxygen saturation, or other biochemical and structural changes to tissue brought on by the onset of disease [13]. In order to perform spectroscopic analysis, some knowledge of the optical pathlength through which light has traveled is required [14]. Time-resolved measurements offer a means to provide such pathlength information, but at the expense of highly specialized equipment [15]. For simpler systems which use continuous-wave (CW) sources, spectroscopy instruments often favour a transmission geometry, with the optical source and detector being placed on opposing sides of

#426627 https://doi.org/10.1364/BOE.426627
Journal © 2021 Received 1 Apr 2021; revised 12 Jun 2021; accepted 13 Jun 2021; published 23 Jun 2021

Biomedical Optics EXPRESS

the sample. For non-scattering/low-scattering samples, the pathlength in this transmission case is well approximated by the physical thickness of the sample.

When investigating samples which strongly scatter light, such as typical biological tissues when probed in the visible to near-infrared range, the average optical pathlength then depends non-trivially on a number of factors including the wavelength, the nature of the scattering structures, and on the total level of absorption. This is problematic since the relationship between the measured attenuation of light and the medium absorption becomes non-linear, significantly increasing the difficulty in analyzing chromophore content. Previous work has employed polarization filtering in an attempt to remedy this problem in the transmission geometry [16], by exploiting the fact that in certain media, photons which preserve their initial polarization state are more likely to have followed straight paths along the transmission axis, thus leaving the pathlength approximately constant for all wavelengths [17]. This allows simple models of attenuation such as the modified Beer-Lambert law to be used under the assumption of a constant optical pathlength as a function of wavelength, which would normally be a poor approximation [18].

In this paper, we are interested in using polarization to improve the accuracy of wide-field diffuse reflectance spectroscopy, where light sources and detectors are arranged to illuminate and collect light on the same side of the sample. This geometry is particularly relevant to the biomedical optics field, where applications seek to characterize the spatial distribution of numerous chromophores (*e.g.* oxy/deoxy-hemoglobin, melanin) in a rapid, low cost, and non-invasive manner. Here, we investigate the use of linear, elliptical, and circular polarization illumination/filters in an analogous manner to Ref. [16], that is, we use polarization gating to enforce a constant effective optical pathlength between measurements made at different wavelengths. The key novelty here is that this is done in the reflection geometry. This geometry presents additional challenges due to the more intricate scattering pathways which photons take between the source and the detector in the reflectance case [19]. However, the use of polarization gating in this geometry has previously been shown to significantly influence the transport of light within scattering media [20,21], suggesting some control over the optical path may still be possible.

In this work, we will present both Monte Carlo simulations, as well as experiments involving phantom media using Intralipid as a scattering medium, with added dyes to represent chromophores of interest. We demonstrate that a significant level of control of the effective optical pathlength can be achieved in the reflection geometry through appropriate choice of polarization channels. We then show that this control can be used to stabilize the optical pathlength over a range of wavelengths, which would otherwise cause the optical pathlength to vary significantly. In Section 2, the modified Beer-Lambert law and the "effective optical pathlength" are introduced and discussed. In Section 3, the experimental setup, capable of performing polarization sensitive reflectance measurements at a number of wavelengths, is described, and the phantom samples are introduced. We then describe the Monte Carlo simulations which demonstrate the impact of polarization gating on the modelled effective optical pathlength, and show that it is possible to select polarization channels which have closely matched effective optical pathlengths at different wavelengths within our samples. In Section 4, using the data from these simulations, a spectroscopic analysis of the measured samples is presented. Finally, in Section 5, we summarize our findings and discuss the potential benefits of diffuse reflectance spectroscopy using tailored polarization gating schemes, and possible practical challenges this may involve.

2. Modified Beer-Lambert law

For a detector measuring monochromatic light of wavelength λ, which has propagated through a scattering and absorbing sample, the measured intensity can be expressed as a weighted integral over all possible attenuated light paths arriving at the detector. Under the assumption of a (locally)

Biomedical Optics EXPRESS

homogeneous distribution of the absorption coefficient, $\mu_a(\lambda)$, this intensity can be expressed as:

$$I_{\text{out}}(\lambda) = I_{\mu_a,0}(\lambda) \int_0^\infty P(\ell) e^{-\mu_a(\lambda)\ell}\, d\ell \tag{1}$$

where we define $I_{\mu_a,0}$ as the intensity measured for a medium with identical scattering properties yet with zero absorbing components (*i.e.* with $\mu_a = 0$), and where $P(\ell)$ is a normalized distribution function describing the probability of photon paths of length ℓ through this non-absorbing medium which reach the detector. Equation (1) is simply a generalization of the well known Beer-lambert law of attenuation due to absorption, only here rather than strictly ballistic trajectories, there are many possible photon paths which may involve numerous scattering events. By "locally homogeneous", we mean that the optical properties of the sample must vary slowly on the scale of the transport mean free path.

In the "modified Beer-Lambert law", we assume that there exists some "effective optical pathlength", L, for which the above expression can be rewritten as:

$$I_{\text{out}}(\lambda) = I_{\mu_a,0}(\lambda) e^{-\mu_a(\lambda)L}\,. \tag{2}$$

Expressed this way, it is evident that the effective optical pathlength, L, must itself have many dependencies [18], including the wavelength, λ, the absorption coefficient of the medium, μ_a, the scattering properties of the medium, and even on any polarization optics involved in the illumination of the medium, or detection of light, as these would each influence the pathlength distribution function, $P(\ell)$. Although at times in this paper we may use a short-hand notation, we should remain mindful that the effective pathlength is dependent on all of these parameters, *i.e.* $L = L(\lambda, \mu_a, P(\ell))$.

In the case where the absorption properties of a medium are due to a number of different chromophores, the absorption coefficient can be expressed as a sum of all such constituents, $\mu_a(\lambda) = \sum \epsilon_n(\lambda)\rho_n$, where $\epsilon_n(\lambda)$ is the absorption coefficient of the n^{th} chromophore, and ρ_n is its concentration within the region of observation. Using the expression for the modified Beer-Lambert law above, we can then define the measured attenuation of the medium due to absorption, $A(\lambda)$, as:

$$A(\lambda) = -log\left[\frac{I_{\text{out}}(\lambda)}{I_{\mu_a,0}(\lambda)}\right] = L(\lambda, \mu_a, P(\ell))\left[\sum_n \epsilon_n(\lambda)\rho_n\right]. \tag{3}$$

The purpose of spectroscopy is to determine the concentration of each chromophore present, ρ_n, by making measurements of the attenuation, $A(\lambda)$, at a number of different wavelengths. The general problem for m-number of measurement wavelengths, and n-number of chromophores, where $m \geq n$, can be expressed as a matrix equation $\vec{A} = \mathbf{L}\,\mathbf{E}\,\vec{\rho}$,

$$\begin{bmatrix} A(\lambda_1) \\ \vdots \\ A(\lambda_m) \end{bmatrix} = \text{diag}\left[L(\lambda_1, \mu_a, P(\ell)), \ldots, L(\lambda_m, \mu_a, P(\ell))\right] \begin{bmatrix} \epsilon_1(\lambda_1) & \cdots & \epsilon_n(\lambda_1) \\ \vdots & \ddots & \vdots \\ \epsilon_1(\lambda_m) & \cdots & \epsilon_n(\lambda_m) \end{bmatrix} \begin{bmatrix} \rho_1 \\ \vdots \\ \rho_n \end{bmatrix}. \tag{4}$$

Here, the concentrations $\vec{\rho} = [\rho_1, \ldots, \rho_n]^T$ may be obtained by computing the pseudo-inverse matrix $[\mathbf{L}\,\mathbf{E}]^+$, which requires us to know the diagonal pathlength matrix $\mathbf{L}$. However, when performing CW spectroscopic examination of an unknown medium, the prior information contained within the pathlength matrix $\mathbf{L}$ is not available. This presents a serious challenge, and forces us to explore methods of either attaining a prior estimate of $\mathbf{L}$ via modelling, or by

Biomedical Optics EXPRESS

attempting to solve the problem in some special scenarios with limited or no prior knowledge. For example, if one considers the special case where the effective optical pathlength in a region of the medium happens to remain constant across all wavelengths, *i.e.* if the matrix $\mathbf{L} = L_c\,\mathbf{I}$, where L_c is constant, and $\mathbf{I}$ is the identity matrix, then the relative concentrations of each chromophore could in fact be determined without explicit knowledge of L_c. In this case, one can solve for $L_c\,\vec{\rho}$, which contains the relative chormophore concentrations. While this special case where $\mathbf{L} = L_c\,\mathbf{I}$ is not met in general (particularly in the backscattering geometry), our intention in this study is precisely to explore the use of polarization gating to enforce this condition.

3. Experimental setup and Monte Carlo simulations

3.1. Experimental setup

In the experimental investigations, a standard setup for wide-field diffuse reflectance spectroscopy was employed, with the addition of polarization optics. As shown in Fig. 1, a white light source (250 W halogen light lamp, KL 2500 LCD, Schott AG, Germany) and narrow bandpass filter (FWHM 10 ± 2 nm, Thorlabs, Germany) at one of three central wavelengths (λ_1 = 532 nm, λ_2 = 570 nm, or λ_3 = 633 nm) is used to illuminate the sample over a large spatial extent. Prior to reaching the sample, the light source is polarized into a specific state of polarization by a combination of a linear polarizer (extinction ratio 10000:1, LPVISB 100, Thorlabs, Germany), and quarter-wave-plate (achromatic zero-order wave-plate for wavelength range 500-700 nm, SPD - Samoylov A.V., Ukraine). On the detection side, a camera (16-bit CMOS camera Orca Flash 4.0 , Hamamatsu Photonics, Japan), with an objective (7000 E, Laser Components SAS, France), and additional magnifying lens, is mounted above and focused at the surface of the sample to record the spatially resolved reflectance. Additional polarization analyzing optics are placed in front of the camera. In this study, measurements were performed on samples by using different polarization "channels". These different polarization channels correspond to one of six illumination states (linear polarized, right-handed elliptically polarized with 10, 20, 30, or 40 degrees of eccentricity, or right-handed circular), and a polarization filter upon detection which is either fully transmissive to the mirror reflection of each illumination state, which we will refer to as "co-polarized", or fully opaque to the mirror reflection state, which we will refer to as "cross-polarized". This results in 12 different polarization channels. In addition, an unpolarized channel is also measured (which can be achieved by summing the measured intensity for the co-linear and cross-linear channels, for example), bringing the total number of measurement channels at each wavelength to 13.

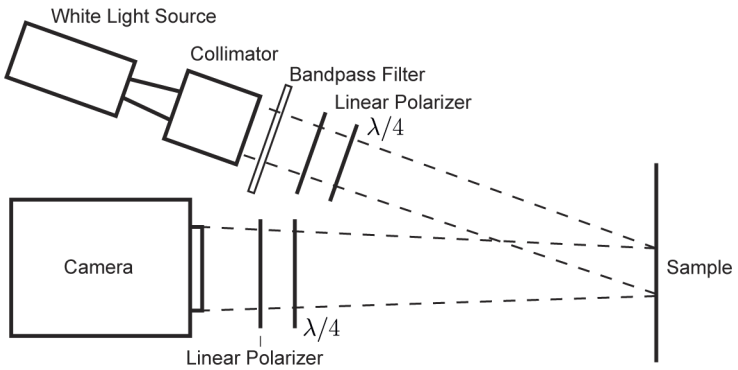

Fig. 1. Experimental setup to perform polarization-gated diffuse reflectance spectroscopy analysis. Quarter-wave-plates are denoted with $\lambda/4$.

Biomedical Optics EXPRESS

3.2. Description of the samples

The samples used in the experiments were liquid solutions of Intralipid (a lipid emulsion), diluted to a concentration of 1% solids by weight. For the purposes of computing the scattering properties of these samples, the lipid scattering particles are assumed to be spherical in shape with an exponential distribution in size, similar to the size distribution measured in Ref. [23] for Intralipid. Specifically, we assumed a normalized number distribution of $N(d) = \alpha e^{-\alpha d}$, where d is the sphere diameter in microns, and $\alpha = 10.9$ is the "rate parameter" characterizing the distribution. The refractive index of the particles was found using the Cauchy dispersion formula employed in Ref. [23] for soybean oil (the main component of the spherical scattering particles in Intralipid, and for the water background: $n(\lambda) = I + J/\lambda^2 + K/\lambda^4$, where $I_{soybean} = 1.451$, $I_{water} = 1.311$, $J = 1.154 \times 10^4$, $K = -1.132 \times 10^9$, and the wavelength, λ, is in nanometers. For the three wavelengths used in our experimental system (532 nm, 570 nm, and 633 nm), the modelled size distribution of spheres is calculated using Mie theory [22] to have the optical properties presented in Table 1, where μ_s is the scattering coefficient, g is the scattering asymmetry parameter (average cosine of the scattering angle), and $\mu_s' = \mu_s(1 - g)$ is the reduced scattering coefficient. As some bottle to bottle variation of Intralipid optical properties is to be expected, the size distribution, refractive index, and resulting scattering properties computed above are an approximation. In Section 4 we will see that the simulated optical pathlength infomation computed using these properties are sufficient to allow for accurate chromophore quantification during spectroscopic analysis of these samples. It is also noted that all samples were prepared and measured at the same time using the same batch of Intralipid so as to minimize any variation between samples.

Table 1. Computed scattering properties of our Intralipid samples diluted to a concentration of 1% solids by weight. Calculated using Mie theory [22], and Intralipid properties found in Ref. [23].

λ	μ_s	Asymmetry, g	μ_s'
532nm	76.0cm^{-1}	0.80	15.2cm^{-1}
570nm	65.0cm^{-1}	0.78	14.3cm^{-1}
633nm	51.2cm^{-1}	0.75	12.8cm^{-1}

Intralipid has negligible absorption over the considered wavelength range. Various quantities of aqueous red and blue dyes were added to each sample to act as the chromophores of interest. The absorption spectra of these dyes are given in Fig. 2. When taking measurements of these samples, we placed four different Intralipid-dye solutions into separate cuvettes and positioned them side by side to be imaged simultaneously by the spectroscopy system, acting as different regions of interest (see Fig. 3). The concentrations of each dye within each cuvette or "region" of the sample, along with the resulting reduced scattering albedos, $a' = \mu_s'/(\mu_s' + \mu_a)$ are given in Table 2.

Table 2. Concentration of aqueous red and blue dye (ρ_1, and ρ_2, respectively) within each of the four cuvettes, given as parts per million (ppm) of dye within the final solution (equivalent to $\mu g/mL$). Also shown are the reduced scattering albedos, $a' = \mu_s'/(\mu_s' + \mu_a)$ for each sample at each of the three wavelengths used.

Sample region	ρ_1 (ppm)	ρ_2 (ppm)	ρ_1/ρ_2 (Red/Blue)	a' (532nm)	a' (570nm)	a' (633nm)
1	1100	1100	1.0	0.974	0.973	0.932
2	2200	1100	2.0	0.953	0.963	0.932
3	3300	1100	3.0	0.932	0.952	0.932
4	4400	1100	4.0	0.912	0.942	0.932

Biomedical Optics EXPRESS

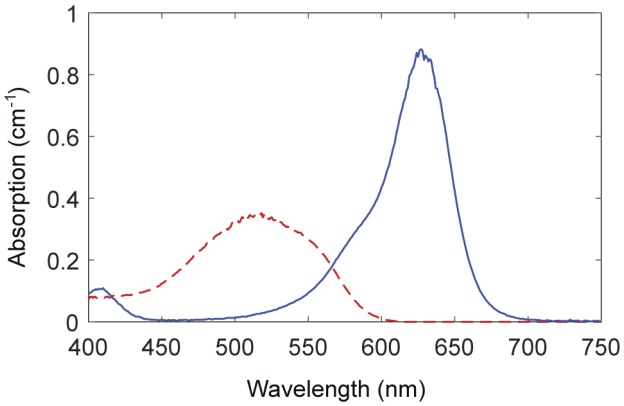

Fig. 2. Absorption spectra $\epsilon_1(\lambda)$ of red dye (dashed red line), and $\epsilon_2(\lambda)$ blue dye (solid blue line) used in experiments. Spectra were measured using an Ocean Optics spectrometer and a 1cm pathlength cuvette. Absorption shown is for aqueous dyes having a concentration of 1000 parts per million (ppm) in water.

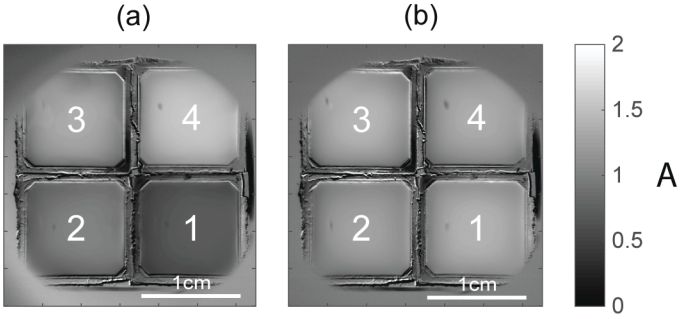

Fig. 3. (a) Attenuation due to absorption, A, of four Intralipid-dye samples measured using the linear cross-polarized channel at 532nm wavelength. (b) Attenuation due to absorption measured using the linear cross-polarized channel at 633nm wavelength. Numbers label each cuvette, or "region" with absorption properties as described in Table 2.

A total of 39 intensity images of the Intralipid-dye samples were taken, corresponding to the 13 different polarization channels for each of the three wavelengths. An additional 39 images were also taken of the Intralipid samples with no dyes present (intensity measurements of $I_{\mu_a,0}$), such that the attenuation due to absorption could be calculated as $A = -\log(I_{\text{out}}/I_{\mu_a,0})$, in accordance with Eq. (3). For each intensity measurement, the intensity is averaged over a 2×2mm region in the center of each cuvette, so as to minimize any dependence on scattering occuring near the edges of the cuvettes. In all cases this ensures the distance from the cuvette edge to the region of observation is greater than 5 transport mean free paths. Two examples of the measured attenuation due to absorption, A, are presented in Fig. 3, where (a) was imaged using the 532nm bandpass filter with the linear cross-polarized channel, and (b) was imaged using the 633nm bandpass filter, also using the linear cross-polarized channel. A full spectroscopic analysis of these samples will be presented in Sec. 4.

3.3. *Monte Carlo simulations*

In order to investigate the wavelength and polarization dependence of the effective optical pathlength L within the Intralipid-dye samples, we employed Monte Carlo simulations for

Biomedical Optics EXPRESS

polarized light using the Intralipid particle size distribution and optical properties calculated in the previous section (Table 1). The simulations were conducted with a program described in previous works [24,25], which uses Mie theory to model each individual scattering event within a slab of scattering material, and the associated changes in polarization state that occur. For each simulation, the total backscattered reflectance reaching the detector from an optically thick slab was calculated for monochromatic illumination normally incident at a single central point in the slab. This method of simulation was chosen for simplicity, as the measured reflectance is proportional (in a homogeneous medium) to wide-field monochromatic illumination and subsequent detection of light exiting at a single point, which is approximately the source-detector geometry that applies to each pixel of the camera in the lab experiments using the setup described in Fig. 1.

In the simulations, the absorption coefficient of the slab was varied between, $0.0\,\mathrm{cm}^{-1} \leq \mu_a \leq 1.6\,\mathrm{cm}^{-1}$, corresponding to the reduced scattering albedos being approximately in the range $0.9 \leq a' \leq 1.0$, adequately covering the range of the Intralipid-dye samples presented in Table 2. Once simulations were completed over the full range of the absorption values for a given wavelength, the simulated attenuation data $A(\lambda, \mu_a)$ were used to compute the effective optical pathlength by differentiating a function which was fitted to $A(\lambda, \mu_a)$. Following Eq. (3), this gives $\partial A(\lambda, \mu_a)/\partial \mu_a = L(\lambda, \mu_a, P(\ell))$. These simulations were repeated using each of the different polarization channels described in the previous section. The polarization filters are handled in the simulations by programming the appropriate Stokes vector for the incident light, and by performing Mueller calculus on the output Stokes vectors.

As an example of the resulting computations, Fig. 4 shows the modelled effective pathlength for each of the three wavelengths using the unpolarized channel (no polarization filters on incidence or detection), displayed as a function of the reduced scattering albedo a' of the simulated slab medium. It can be seen that indeed the effective pathlength in the simulated medium has a strong dependence on the total level of absorption (and thus the albedo), and as expected, the greatest values of L are at an albedo value of $a' = 1$, where there is no absorption acting to attenuate the longer photon paths contributing to the signal. In addition, the blue (532 nm) wavelength shows the shortest overall pathlengths, as the scattering coefficient is the highest for this wavelength, resulting in lower penetration of the incident light. Also marked as crosses on Fig. 4 are the albedos and effective pathlengths corresponding to region 1 of the Intralipid-dye samples described in the previous section (with dye ratio $\rho_1/\rho_2 = 1.0$). It can be seen that by simply changing the wavelength of light used to illuminate the sample, the modelled optical pathlength in the sample can vary greatly, due to the different scattering response of the medium at each wavelength, as well as the implicit change in albedo resulting from each dye's absorption spectrum. This change is particularly noticeable when switching to the red wavelength ($\lambda = 633$ nm), as the effective pathlength (red cross) drops significantly in this particular sample compared to the 570 nm and 532 nm wavelengths (orange and blue crosses).

In addition to the unpolarized measurement channel, we analyzed the simulated pathlength data obtained from the remaining 12 polarization channels. It was observed that the effective pathlength L also changes significantly depending on the particular polarization channel selected. The most clearly observed differences were between the co-linear and cross-linear channels, shown in Fig. 5(a). As expected, the "co-linear" channel has the shortest effective pathlength, as this channel is dominated by light which scatters only superficially, largely maintaining its polarization and allowing it to pass through the co-alligned linear polarization filter in front of the detector. The cross-linear signal on the other hand, which filters out the directly reflected light from superficial surface layers, results largely from light which has significantly altered its polarization state, typically corresponding to further propagation distances within the sample. The unpolarized channels from the previous figure (Fig. 4) fell intermediate to these two extremes. The co-circular, and cross-circular channels demonstrated an interesting variation of pathlength,

Biomedical Optics EXPRESS

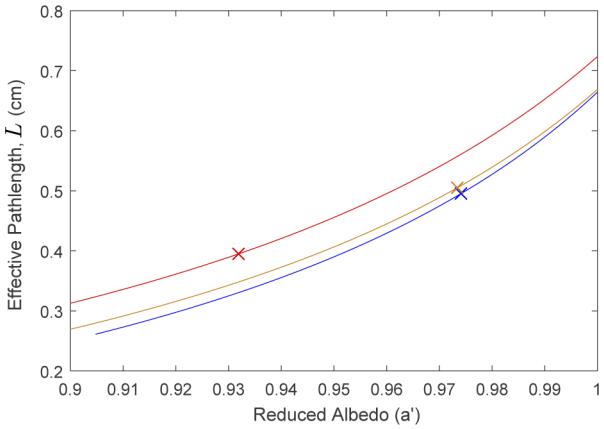

Fig. 4. Effective pathlength L as a function of the reduced scattering albedo for the unpolarized measurement channel. 532 nm, 570 nm, and 633 nm wavelengths are represented as blue, orange, and red lines, respectively. Cross marks on each curve represent the effective optical pathlength in the Intralipid-Dye region 1 at each wavelength, determined by that samples wavelength dependent reduced albedo (see Table 2).

with each exhibiting a crossover at some value of the reduced albedo, see Fig. 5(b). This indicates that for such polarization channels, the pathlength depends much more dynamically on the medium scattering properties, likely including the scattering asymmetry and circular polarization memory [9], which makes defining a consistent trend difficult. Additionally, the pathlength of various elliptical channels (not shown here), fell in the intermediate range between the co-linear, and cross-linear channels.

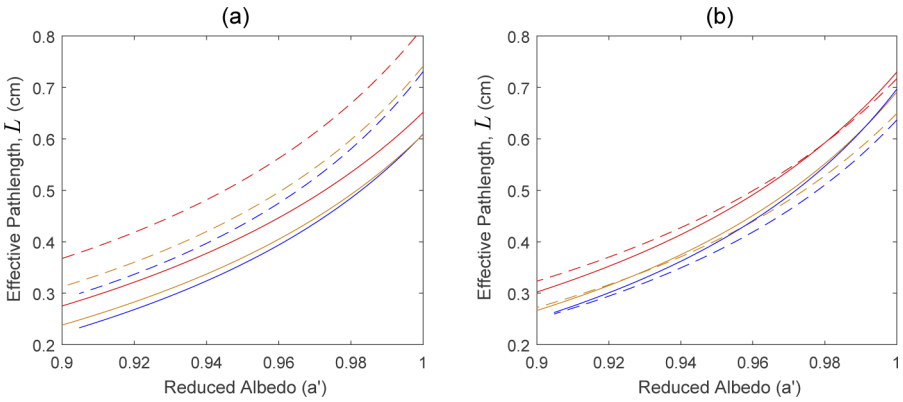

Fig. 5. (a) Monte Carlo modelled effective pathlength L as a function of the reduced scattering albedo for co-linear (solid), and cross-linear (dashed) channels. (b) Effective pathlength as a function of the reduced scattering albedo for co-circular (solid), and cross-circular (dashed) channels. 532 nm, 570 nm, and 633 nm wavelengths are represented as blue, orange, and red lines, respectively.

The important observation from the above figures is that the variation in the effective pathlength caused by a change in wavelength (both due to the changing scattering properties, and the implicit change in the albedo), is in some cases comparable in magnitude to the change in pathlength caused by altering the polarization imaging channel. This suggests that if the effect of changing polarization is well understood for a given medium, then polarization gating could be used

Biomedical Optics EXPRESS

to counter the effects of wavelength induced changes to the pathlength, thus maintaining a near-constant pathlength over the wavelength range used (making spectroscopic analysis easier). In fact, there exist numerous situations, with various polarization channels, for which the effective pathlengths are similar across all three wavelengths within the considered Intralipid-dye samples. One such example is given in Fig. 6(a), showing the modelled pathlengths as a function of the reduced albedo for the co-linear channel at 532 nm, the co-linear channel at 570 nm, and the cross-linear channel at 633 nm. Also marked as crosses on the figure are the values of the reduced albedo corresponding to the Intralipid-dye sample region 1 (see Table 2 for the albedos at each wavelength). It can be seen that the effective pathlengths for this region of the sample at each wavelength are nearly equivalent (same height on the graph), much closer together than the unpolarized channels shown in Fig. 4. This means that although the scattering and absorbing properties of the medium are changing significantly by changing the illumination wavelength, this particular combination of polarization channels have almost exactly counteracted these effects, and resulted in near identical effective optical pathlengths. In Fig. 6(b), another example is given, this time for the cross-elliptical channel with 20 degrees ellipticity at 532 nm, the co-linear channel at 570 nm, and the cross-elliptical channel with 30 degrees ellipticity at 633 nm. Also marked as crosses on the figure are the locations corresponding to the albedos within the Intralipid-dye region 2. Here again, this particular combination is seen to have closely matched effective pathlengths, demonstrating the possibility of using polarization to enforce this condition in the backscattering geometry.

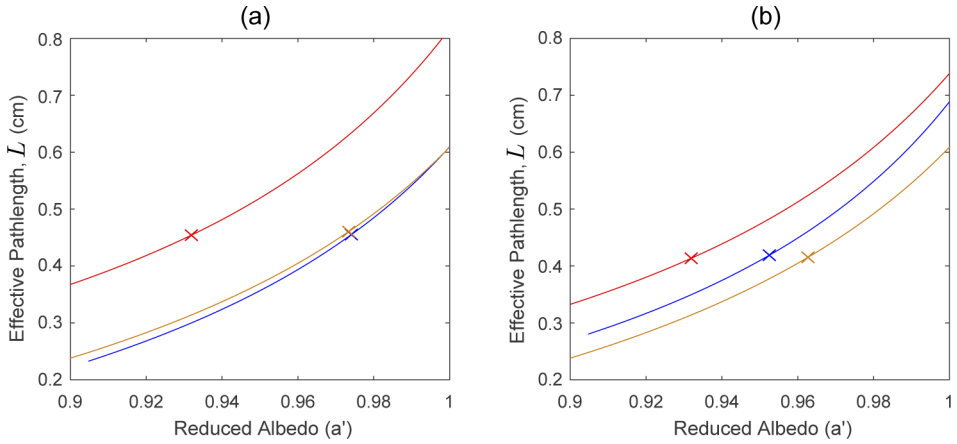

Fig. 6. (a) - Monte Carlo modelled effective pathlength L as a function of the reduced scattering albedo for co-linear channel at 532 nm (blue line), co-linear channel at 570 nm (orange line), and cross-linear channel at 633 nm (red line). Marks on each curve represent the optical pathlength in the Intralipid-dye region 1 at each wavelength (see Table 2 for the albedos). (b) Effective pathlength L as a function of the reduced scattering albedo for the cross-elliptical channel with 20 degrees ellipticity at 532 nm (blue line), co-linear channel at 570 nm (orange line), and cross-elliptical channel with 30 degrees ellipticity at 633 nm (red line). Marks on each curve represent the optical pathlength in the Intralipid-dye region 2 at each wavelength (see Table 2 for the albedos).

4. Spectroscopy results

In this section we carry out a complete spectroscopic analysis of the Intralipid-dye samples introduced in Section 3.2, and make use of the Monte Carlo modelling from Section 3.3. Referring again to the general formulation of the problem detailed in Eq. (4), in the examples presented in this study we use $m = 3$ different measurement wavelengths (532nm, 570nm, 633nm) to

Biomedical Optics EXPRESS

attain information of $n = 2$ different chromophore concentrations (red dye ρ_1, and blue dye ρ_2). Additionally, absorption measurements at each wavelength can be made using any one of the 13 available polarization channels, thus there are in fact $13^3 = 2197$ possible ways to formulate the matrix expression in Eq. (4). In order to fully investigate the influence of the various polarization channel combinations on the outcome of the spectroscopic analysis, we evaluate the problem for each of these possibilities, and attain 2197 separate approximations of the ratio of the two dye concentrations (ρ_1/ρ_2) for each of the four regions of the Intralipid-dye samples.

The results of the spectroscopic analysis are presented in Fig. 7. The analysis in Fig. 7(a) is performed using the Monte Carlo simulated values of the effective pathlengths to construct each possible pathlength matrix $\mathbf{L}$. Then, as an alternative approach, in Fig. 7(b) we repeat the evaluation of the problem without the Monte carlo prior information, and instead make the assumption of a constant effective optical pathlength for all wavelengths and polarization channels (*i.e.* assuming $\mathbf{L} = L_c\,\mathbf{I}$, for some unknown L_c). The results are displayed such that each point represents the recovered ratio of red dye and blue dye (ρ_1/ρ_2) using one of the possible 2197 combinations of polarization channels and measurement wavelengths. The horizontal axis represents the disagreement between the effective optical pathlengths for each estimate, measured as the standard deviation (SD) between the three Monte Carlo modelled pathlengths in each sample region for the corresponding set of three polarization measurement channels. Here, a high standard deviation corresponds to the modelled pathlengths being very different from each other, whilst a low standard deviation corresponds to polarization measurement channel combinations which happen to have very similar optical pathlengths in the sample, such as the examples shown

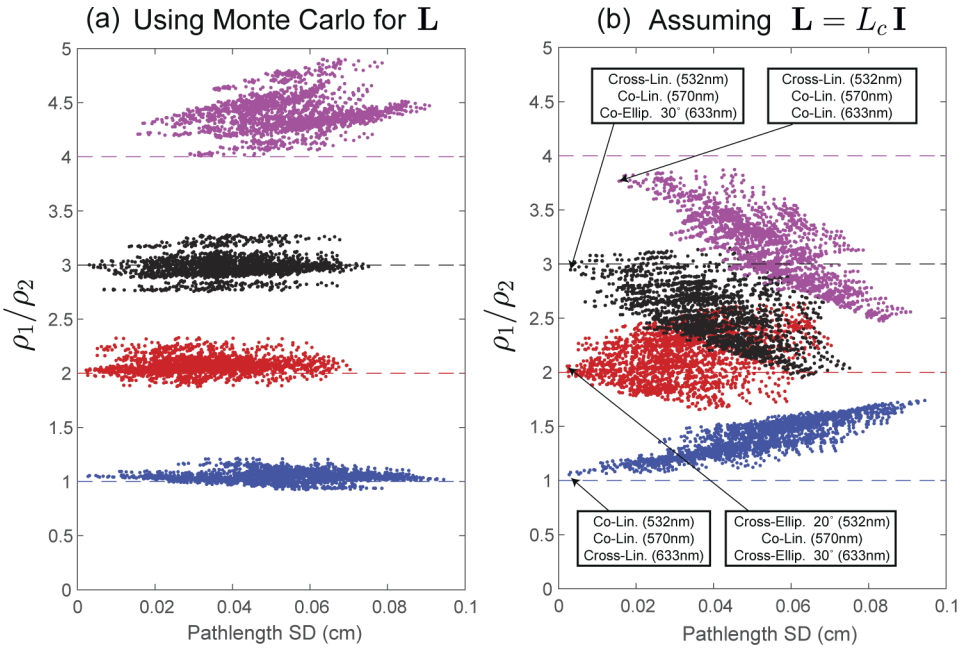

Fig. 7. (a) - Ratio of red and blue dye ρ_1/ρ_2 vs. pathlength standard deviation (SD) from measurements of each of the four Intralipid-dye regions, using Monte Carlo data to form the pathlength matrix $\mathbf{L}$. (b) - Ratio of red and blue dye ρ_1/ρ_2 vs. pathlength standard deviation (SD) from measurements of each of the four Intralipid-dye regions, using the approximation $\mathbf{L} = L_c\,\mathbf{I}$. Each colored point represents one of the possible 2197 combinations of polarization channels used in Eq. (4). Known values of ρ_1/ρ_2 for Intralipid-dye sample regions 1, 2, 3 & 4 shown as Blue, Red, Black, Purple dashed lines, respectively.

Biomedical Optics EXPRESS

in Fig. 6. A summary of the average estimated values of the chromophore concentration ratios for both Fig. 7(a) and (b) is given in Table 3. Also included in this table are the average values of the absolute concentration of each dye recovered using the method with Monte Carlo prior information. Note however, that due to the assumption of constant unknown pathlength in the alternate method, the absolute concentration values are not available (only the ratio ρ_1/ρ_2 is recoverable when assuming $\mathbf{L} = L_c\mathbf{I}$).

Table 3. Average spectroscopic results of all possible polarization channel combinations for the four regions of the sample using Monte Carlo (MC) data for the pathlength matrices L. Red and blue dye concentrations given as parts per million (ppm), along with their concentration ratios (ρ_1/ρ_2). Last column shows results without using Monte Carlo data, under the assumption of a constant pathlength for all cases, with $\mathbf{L} = L_c\,\mathbf{I}$. True values of ρ_1 and ρ_2 are given in Table 2.

Sample / Region	ρ_1 (MC) (ppm)	ρ_2 (MC) (ppm)	ρ_1/ρ_2 (MC)	ρ_1/ρ_2 (Assuming $\mathbf{L} = L_c\,\mathbf{I}$)
1	1160 ± 28	1109 ± 33	1.05 ± 0.04	1.39 ± 0.13
2	2163 ± 37	1045 ± 26	2.07 ± 0.06	2.14 ± 0.19
3	3413 ± 35	1144 ± 30	2.98 ± 0.08	2.52 ± 0.25
4	4899 ± 66	1116 ± 33	4.39 ± 0.14	3.11 ± 0.29

5. Discussion and summary

Referring to Fig. 7(a), where Monte Carlo prior information was used in the analysis, we observe that the points cluster around the lines corresponding to the true values of $\rho_1/\rho_2 = 1, 2, 3, \& 4$, for the Intralipid-dye sample regions 1, 2, 3 & 4, respectively. Here it is also observed that as the pathlength standard deviation (SD) increases, this does not greatly alter the distribution of the recovered values of ρ_1/ρ_2, particularly for sample regions 1-3. This indicates that the Monte Carlo modelled pathlengths are reasonably accurate within each sample and are appropriately scaling the attenuation measurements in each case in order to accurately recover the underlying choromophore concentrations. Comparing Tables 2 and 3, the mean error in the recovered values of ρ_1/ρ_2 is no greater than 5% for sample regions 1-3, and approximately 10% for sample region 4.

In Fig. 7(b) where the Monte Carlo modelled pathlengths are omitted from the analysis (where we instead assume $\mathbf{L} = L_c\,\mathbf{I}$ for some unknown L_c), it is obvious that as the pathlength standard deviation increases, the estimated chromophore ratio ρ_1/ρ_2 tends to deviate significantly from the true values. This is because as the pathlength standard deviation increases, the underlying assumption of equal pathlengths breaks down significantly, leading to large errors in the estimated chromophore concentrations. Comparing Tables 2 and 3, the mean error in the recovered values of ρ_1/ρ_2 in all four regions of the sample are higher than in the case where Monte Carlo prior information was used, with the mean error being as large as 39% for sample region 1.

If however we happen to choose combinations of polarization channels which have very similar effective optical pathlengths over the three wavelengths (low pathlength standard deviation), then Fig. 7(b) demonstrates that the ratio of chromophore concentrations can still be estimated accurately, and without requiring explicit prior knowledge of the optical pathlengths. The specific combinations of polarization channels with the most similar pathlengths within each of the four sample regions are highlighted on the figure, where the highlighted examples shown for sample regions 1 and 2 are the same combinations demonstrated in Fig. 6(a) and 6(b), respectively. Using these polarization channel combinations resulted in an error of less than 7% in the estimation of ρ_1/ρ_2. In general, the type of polarization channel combinations with low pathlength standard deviation appear to be specific to each sample region, with no clear trend being observed which applied to all four sample regions.

Biomedical Optics EXPRESS

As an additional observation, we see that for sample region 4, the minimum pathlength standard deviation is not as low as in the other three samples. This suggests that for some media, the selection of polarization channels does not offer enough control over the effective pathlengths at each wavelength to make the them all similar. This shows that there certainly exists a limit to how different the optical properties of a medium can be at each wavelength, and still successfully apply polarization gating to improve accuracy in this manner.

To summarize, in this study, the influence of polarization gating on the effective optical pathlength within scattering and absorbing media was explored, and we applied our findings towards continuous-wave reflectance spectroscopy. First, using a polarization capable Monte Carlo model, we demonstrated that the effective optical pathlength in reflectance-mode imaging varies significantly when altering the polarization channel. It was also clearly demonstrated that combinations of polarization channels exist which have very similar effective optical pathlengths over a range of wavelengths within the Intralipid-dye samples we investigated. Secondly, it was demonstrated that these particular polarization channel combinations could be used in Eq. (4) without explicitly requiring the pathlengths as an input (under the assumption that $\mathbf{L} = L_c\mathbf{I}$, for some unknown L_c), and that this method still performed to a similar level of accuracy as the measurements which took full advantage of the prior information afforded by the Monte Carlo simulations. However, this raises the question of how to select the ideal combination of polarization channels at each wavelength in practice. In other words, whilst we are eliminating the need for explicit prior pathlength information to be included in the analysis (when solving Eq. (4)), it introduces another requirement that the ideal polarization channels be selected which have similar effective pathlengths. Whilst it is possible that with further investigation in various samples, a sample specific calibration of polarization channels could be applied successfully, this may remain a significant challenge in practice.

It should also be mentioned that imaging and sensing with polarized light is not only of interest to the biomedical optics community. Applications exist in various fields such as remote sensing of aerosols, clouds, and atmospheric dust [26], or imaging underwater [27], each of which can exploit the influence that polarization gating imposes on light transport. In any such relevant domain, another plausible benefit of being able to select polarization channels which control the effective optical pathlength within a medium, versus numerically accounting for pathlength differences (e.g. with Monte Carlo prior pathlength information), is that in the former case the physical region of the sample begin probed is likely to be more similar. This may be an advantage in any situation where it is important to keep this probed region constant. In the case of spectroscopy, it is important to keep the probed region constant as we change the optical wavelength, particulary if there are spatial inhomogeneities in the medium. However, this could also apply to situations in which it is important to maintain a constant probing volume whilst the scattering medium is changing temporally.

As a final point, it should also be noted that if a full Mueller Matrix characterization of the medium has been attained by the camera at each wavelength, then the required attenuation measurements corresponding to any arbitrary polarization imaging channel can be recovered post-measurement [28]. This means that the ideal combination of polarization channels need not be known at the time of measurement, but could be calibrated as a post-process.

Disclosures. No conflicts of interest, financial or otherwise, are declared by the authors.

Data availability. Data underlying the results presented in this paper are not publicly available at this time but may be obtained from the authors upon reasonable request.

References

1. S. Demos and R. Alfano, "Optical polarization imaging," Appl. Opt. **36**(1), 150–155 (1997).
2. A. Pierangelo, A. Benali, M.-R. Antonelli, T. Novikova, P. Validire, B. Gayet, and A. De Martino, "Ex-vivo characterization of human colon cancer by mueller polarimetric imaging," Opt. Express **19**(2), 1582–1593 (2011).
3. M. P. Siegel, Y. L. Kim, H. K. Roy, R. K. Wali, and V. Backman, "Assessment of blood supply in superficial tissue by polarization-gated elastic light-scattering spectroscopy," Appl. Opt. **45**(2), 335–342 (2006).

Biomedical Optics EXPRESS

4. F. C. MacKintosh, J.-X. Zhu, D. Pine, and D. Weitz, "Polarization memory of multiply scattered light," Phys. Rev. B **40**(13), 9342–9345 (1989).
5. D. Bicout, C. Brosseau, A. S. Martinez, and J. M. Schmitt, "Depolarization of multiply scattered waves by spherical diffusers: Influence of the size parameter," Phys. Rev. E **49**(2), 1767–1770 (1994).
6. A. D. Kim and M. Moscoso, "Backscattering of circularly polarized pulses," Opt. Lett. **27**(18), 1589–1591 (2002).
7. M. Xu and R. Alfano, "Circular polarization memory of light," Phys. Rev. E **72**(6), 065601 (2005).
8. P. Shukla, R. Sumathi, S. Gupta, and A. Pradhan, "Influence of size parameter and refractive index of the scatterer on polarization-gated optical imaging through turbid media," J. Opt. Soc. Am. A **24**(6), 1704–1713 (2007).
9. C. M. Macdonald, "Characterizing the depolarization of circularly polarized light in turbid scattering media," J. Opt. Soc. Am. A **35**(12), 2104–2110 (2018).
10. V. Sankaran, M. J. Everett, D. J. Maitland, and J. T. Walsh, "Comparison of polarized-light propagation in biological tissue and phantoms," Opt. Lett. **24**(15), 1044–1046 (1999).
11. M.-R. Antonelli, A. Pierangelo, T. Novikova, P. Validire, A. Benali, B. Gayet, and A. De Martino, "Impact of model parameters on monte carlo simulations of backscattering mueller matrix images of colon tissue," Biomed. Opt. Express **2**(7), 1836–1851 (2011).
12. M. Ahmad, S. Alali, A. Kim, M. F. Wood, M. Ikram, and I. A. Vitkin, "Do different turbid media with matched bulk optical properties also exhibit similar polarization properties?" Biomed. Opt. Express **2**(12), 3248–3258 (2011).
13. I. J. Bigio and J. R. Mourant, "Ultraviolet and visible spectroscopies for tissue diagnostics: fluorescence spectroscopy and elastic-scattering spectroscopy," Phys. Med. Biol. **42**(5), 803–814 (1997).
14. D. T. Delpy, M. Cope, P. van der Zee, S. Arridge, S. Wray, and J. Wyatt, "Estimation of optical pathlength through tissue from direct time of flight measurement," Phys. Med. Biol. **33**(12), 1433–1442 (1988).
15. P. Taroni, A. Pifferi, A. Torricelli, D. Comelli, and R. Cubeddu, "In vivo absorption and scattering spectroscopy of biological tissues," Photochem. Photobiol. Sci. **2**(2), 124–129 (2003).
16. I. M. Stockford, B. Lu, J. A. Crowe, S. P. Morgan, and D. E. Morris, "Reduction of error in spectrophotometry of scattering media using polarization techniques," Appl. Spectrosc. **61**(12), 1379–1389 (2007).
17. J. Schmitt, A. Gandjbakhche, and R. Bonner, "Use of polarized light to discriminate short-path photons in a multiply scattering medium," Appl. Opt. **31**(30), 6535–6546 (1992).
18. A. Sassaroli and S. Fantini, "Comment on the modified beer–lambert law for scattering media," Phys. Med. Biol. **49**(14), N255–N257 (2004).
19. C. M. Gardner, "Transmission versus reflectance spectroscopy for quantitation," J. Biomed. Opt. **23**, 018001 (2018).
20. S. Sridhar and A. Da Silva, "Enhanced contrast and depth resolution in polarization imaging using elliptically polarized light," J. Biomed. Opt. **21**(7), 071107 (2016).
21. S. Rehn, A. Planat-Chrétien, M. Berger, J.-M. Dinten, C. Deumié-Raviol, and A. da Silva, "Depth probing of diffuse tissues controlled with elliptically polarized light," J. Biomed. Opt. **18**(1), 016007 (2013).
22. C. F. Bohren and D. R. Huffman, *Absorption and Scattering of Light by Small Particles* (John Wiley & Sons, 2008).
23. H. J. Van Staveren, C. J. Moes, J. van Marie, S. A. Prahl, and M. J. Van Gemert, "Light scattering in lntralipid-10% in the wavelength range of 400–1100 nm," Appl. Opt. **30**(31), 4507–4514 (1991).
24. U. Tricoli, C. M. Macdonald, A. Da Silva, and V. A. Markel, "Reciprocity relation for the vector radiative transport equation and its application to diffuse optical tomography with polarized light," Opt. Lett. **42**(2), 362–365 (2017).
25. C. M. Macdonald, U. Tricoli, A. Da Silva, and V. A. Markel, "Numerical investigation of polarization filtering for direct optical imaging within scattering media," J. Opt. Soc. Am. A **34**(8), 1330–1338 (2017).
26. J. Van der Laan, D. Scrymgeour, S. Kemme, and E. Dereniak, "Detection range enhancement using circularly polarized light in scattering environments for infrared wavelengths," Appl. Opt. **54**(9), 2266–2274 (2015).
27. G. D. Gilbert and J. C. Pernicka, "Improvement of underwater visibility by reduction of backscatter with a circular polarization technique," Appl. Opt. **6**(4), 741–746 (1967).
28. A. Lizana, A. Van Eeckhout, K. Adamczyk, C. Rodríguez, J. C. Escalera, E. Garcia-Caurel, I. Moreno, and J. Campos, "Polarization gating based on mueller matrices," J. Biomed. Opt. **22**(05), 1 (2017).